

Spin Seebeck Effect in Normal-Metal–Chiral-Insulator Heterostructure

Jiayan Zhang,¹ Gaoyang Li,² Gaomin Tang,^{3,*} and Yanxia Xing^{1,†}

¹Key Laboratory of Advanced Optoelectronic Quantum Architecture and Measurement,
Ministry of Education, Beijing Institute of Technology, Beijing 100081, China

²School of Physics & Information Science, Shaanxi University of Science & Technology, Xi'an 710021, China

³Graduate School of China Academy of Engineering Physics, Beijing 100193, China

Phonons can carry angular momentum and exhibit chirality through the circular polarization of atomic motion. This enables a phonon-mediated spin Seebeck effect (SSE) via the conversion of phonon angular momentum into electron spin angular momentum. In this Letter, we develop a theoretical framework for calculating the spin current in a normal-metal–chiral-insulator (NM–CI) heterostructure within the nonequilibrium Green’s function formalism. We discuss the influence of (i) the thermal bias across the NM–CI interface, (ii) the chemical potential of the NM, and (iii) the modification of the interfacial on-site potential on the spin transport properties. We identify two characteristic nonlinear spin-transport phenomena: negative differential SSE and spin-current rectification. The negative differential SSE arises from the competition between the thermal bias and the density of thermally excited electrons. Spin-current rectification suggests the possibility of realizing a thermally controlled spin diode. We also find that the spin-transport behavior is closely associated with an effective interfacial spectral density. This work suggests a novel route toward thermally controlled spintronic devices using chiral phonons.

Introduction—A central goal of spintronics is to control and manipulate spin currents—the transport of electron spin angular momentum—in solid-state systems [1–3]. In addition to conduction electrons that carry spin angular momentum in metals and semiconductors, spin waves (magnons), the collective excitations of localized magnetic moments, can also transfer spin angular momentum even in ferromagnetic insulators (FIs) [4, 5]. Magnon spin currents can be generated by microwave irradiation or by applying a temperature gradient across the FI; these mechanisms are known as spin pumping and the spin Seebeck effect (SSE) [6–12], respectively. The resulting spin current can be detected in an adjacent normal metal (NM) via the inverse spin Hall effect [12–15]. Magnon spin transport has also been widely studied in FI–NM [16–21], FI–superconductor [22–24], antiferromagnet–NM [25–27], and altermagnet systems [28–30].

Phonons, the quanta of lattice vibrations, are extensively discussed in the fields of superconductivity [31], thermal transport [32–36], and nanophotonics [37–39]. In many conventional treatments, phonons are described as linearly polarized lattice vibrations. Recent theoretical and experimental studies have shown that atoms in solids can undergo circularly polarized motion, indicating that phonons can carry angular momentum and exhibit chirality [40–50]. Phonon chirality can give rise to a variety of intriguing transport phenomena, such as chirality-induced selectivity of phonon angular momenta [51], phonon Edelstein effect [52], chiral-phonon-induced spin transport [53], chiral-phonon diode effect [54], orbital Seebeck effect [55], and SSE due to spin-phonon conversion [56–58]. However, nonlinear transport phenomena associated with the chiral-phonon-mediated SSE remain largely unexplored. In this Letter, we employ the

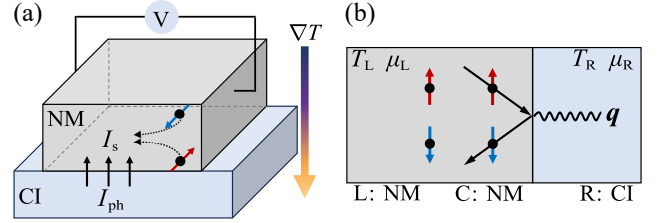


FIG. 1. (a) Schematic of the experimental device. The temperature gradient ∇T is perpendicular to the NM–CI interface. The black arrows at the interface denote the conversion of the phonon angular momentum current I_{ph} into the spin current I_s . Electrons in the NM are shown as black solid circles, with blue (red) arrows indicating the spin orientations. The black dotted lines with arrows are electron trajectories arising from spin-dependent scattering. (b) Schematic of the two-terminal representation of the NM–CI heterostructure, consisting of an NM left lead, an NM central region, and a CI phonon reservoir. T_L (T_R) and μ_L (μ_R) are the temperature and chemical potential of the left (right) lead, respectively. The black straight lines with arrows represent electrons before and after scattering, and the wavy line denotes phonon emission or absorption at the interface.

nonequilibrium Green’s function formalism to investigate two characteristic nonlinear effects in this setting: the negative differential SSE and spin-current rectification. The experimental setup consists of a chiral insulator (CI) adjacent to an NM, with a temperature gradient ∇T applied perpendicular to the NM–CI interface, as shown in Fig. 1. The thermally activated phonon angular momentum (phAM) current in the CI is converted into an electron spin current in the adjacent NM via interfacial spin-phonon conversion between the chiral phonons in the CI and the electrons in the NM. Counterpropagating electrons with opposite spins in the NM are scattered toward the same side [black dotted line with arrows in

Fig. 1(a)]. As a result, an electron imbalance builds up between the two sides, leading to a measurable potential drop.

Model and Hamiltonian—In this Letter, we develop a framework for calculating the spin current in an NM using the nonequilibrium Green’s function formalism [59–61]. To model the SSE in the NM–CI system, we consider a two-terminal setup shown in Fig. 1(b). The total Hamiltonian reads

$$\mathcal{H} = \mathcal{H}_L + \mathcal{H}_C + \mathcal{H}_T + \mathcal{H}_{\text{ph}} + \mathcal{H}_{e\text{-ph}}. \quad (1)$$

Here $\mathcal{H}_L = \sum_{\mathbf{k}\sigma} \epsilon_{\mathbf{k}\sigma} b_{\mathbf{k}\sigma}^\dagger b_{\mathbf{k}\sigma}$ is the Hamiltonian of the left lead, where $b_{\mathbf{k}\sigma}^\dagger$ ($b_{\mathbf{k}\sigma}$) is the creation (annihilation) operator for an electron with wave vector \mathbf{k} and spin σ . We Fourier-transform \mathcal{H}_L and obtain the corresponding lattice Hamiltonian as $H_L = 2t\ell \sum_{i\sigma} b_{i\sigma}^\dagger b_{i\sigma} - t \sum_{(ij)\sigma} b_{i\sigma}^\dagger b_{j\sigma}$, where $\ell = 1, 2, 3$ denotes the dimensionality and $t = 21.768$ meV is the hopping parameter. $\mathcal{H}_C = \sum_{n\sigma} \epsilon_{n\sigma} c_{n\sigma}^\dagger c_{n\sigma}$ is the Hamiltonian of the central region, where $c_{n\sigma}^\dagger$ ($c_{n\sigma}$) creates (annihilates) an electron with energy $\epsilon_{n\sigma}$. $\mathcal{H}_T = \sum_{n\mathbf{k}\sigma} (t_{n\mathbf{k}\sigma} c_{n\sigma}^\dagger b_{\mathbf{k}\sigma} + \text{h.c.})$ describes the coupling between the left lead and the central region, where the tunneling matrix element is set to $t_{n\mathbf{k}\sigma} = t = 21.768$ meV in our calculations. $\mathcal{H}_{\text{ph}} = \sum_{\mathbf{q}\lambda} \hbar\omega_{\mathbf{q}\lambda} (a_{\mathbf{q}\lambda}^\dagger a_{\mathbf{q}\lambda} + 1/2)$ is the Hamiltonian of the chiral phonons in the right lead, where $a_{\mathbf{q}\lambda}^\dagger$ ($a_{\mathbf{q}\lambda}$) is the phonon creation (annihilation) operator with wave vector \mathbf{q} and polarization λ , and $\lambda = \pm$ labels the left- and right-circularly polarized modes. By considering the spin-microrotation coupling between electron spins in the NM and chiral phonons in the CI, the electron-phonon interaction $\mathcal{H}_{e\text{-ph}}$ is written as [57]

$$\mathcal{H}_{e\text{-ph}} = - \sum_{n\mathbf{q}\lambda} \left(\mathcal{J}_{qn} d_{\mathbf{q}\lambda}^\dagger c_{n\downarrow}^\dagger c_{n\uparrow} + \mathcal{J}_{qn}^* d_{\mathbf{q}\lambda} c_{n\uparrow}^\dagger c_{n\downarrow} \right). \quad (2)$$

Here \mathcal{J}_{qn} denotes the electron-phonon coupling strength. $d_{\mathbf{q}\lambda}^\dagger = \eta_{\mathbf{q}\lambda} (a_{\mathbf{q}\lambda} - a_{-\mathbf{q}\bar{\lambda}}^\dagger)$ and $d_{\mathbf{q}\lambda} = \eta_{\mathbf{q}\lambda}^* (a_{\mathbf{q}\lambda}^\dagger - a_{-\mathbf{q}\bar{\lambda}})$ are the vorticity creation and annihilation operators with $\bar{\lambda} = -\lambda$, where $\eta_{\mathbf{q}\lambda} = \sqrt{\hbar\omega_{\mathbf{q}\lambda}/(2\rho V)} [(\mathbf{q} \times \mathbf{e}_{\mathbf{q}\lambda})_x + i(\mathbf{q} \times \mathbf{e}_{\mathbf{q}\lambda})_y]$ characterizes the propagation and polarization of chiral phonons [57]. The interaction Hamiltonian in Eq. (2) illustrates the following scattering process: a spin-up (down) electron is scattered into a spin-down (up) state, accompanied by an increase (decrease) in phonon vorticity. This process is crucial for spin-phonon conversion and thus for the generation of spin currents in the NM.

Derivation of the spin-current expression—The system carries no net charge current because the right lead is insulating. However, the system can carry a spin current due to the interfacial spin-phonon conversion. The spin current in the left lead is defined as

$$I_s = \frac{\hbar}{2e} (I_\uparrow^e - I_\downarrow^e), \quad (3)$$

where the spin-dependent charge current I_σ^e is [59, 62]

$$I_\sigma^e = \frac{e}{\hbar} \int \frac{dE}{2\pi} \text{Tr} [\mathbf{G}_\sigma^>(E) \Sigma_{L\sigma}^<(E) - \mathbf{G}_\sigma^<(E) \Sigma_{L\sigma}^>(E)]. \quad (4)$$

Boldface Latin and Greek letters denote matrices whose indices label lattice sites. $\mathbf{G}_\sigma^>/<$ are the greater and lesser electron Green’s functions of the central region. The retarded self-energy due to the left lead is $\Sigma_{L\sigma}^r(E) = \mathbf{H}_T^\dagger \mathbf{g}_{L\sigma}^r(E) \mathbf{H}_T$, where \mathbf{H}_T is the tunneling matrix between the left lead and the central region, and the left-lead surface Green’s function $\mathbf{g}_{L\sigma}^r$ is calculated from the left-lead lattice Hamiltonian H_L using the iterative scheme [63, 64]. The linewidth function of the left lead is $\Gamma_{L\sigma}(E) = i[\Sigma_{L\sigma}^r(E) - \Sigma_{L\sigma}^a(E)]$. For the left lead, $\Sigma_{L\sigma}^>(E) = i[f_L(E) - 1]\Gamma_{L\sigma}(E)$ and $\Sigma_{L\sigma}^<(E) = i f_L(E) \Gamma_{L\sigma}(E)$ where $f_L(E) = 1/[e^{(E-\mu_L)/(k_B T_L)} + 1]$ is the Fermi–Dirac distribution.

The spin current can be calculated once we obtain the central-region Green’s functions. The greater/lesser and retarded Green’s functions in the central region are given by [see the Supplemental Material [65] for details of the derivation]

$$\mathbf{G}_\sigma^>/<(E) = \mathbf{G}_\sigma^r(E) [\Sigma_{L\sigma}^>/<(E) + \bar{\Sigma}_{R\sigma}^>/<(E)] \mathbf{G}_\sigma^a(E), \quad (5)$$

$$\mathbf{G}_\sigma^r(E) = [E\mathbf{I} - \mathbf{H}_C - \Sigma_{L\sigma}^r(E) - \bar{\Sigma}_{R\sigma}^r(E)]^{-1}. \quad (6)$$

Here, \mathbf{I} is the unit matrix. $\Sigma_{L\sigma}$ is the left-lead self-energy. $\bar{\Sigma}_{R\sigma}$ is the phononic self-energy and is expressed as [65]

$$\bar{\Sigma}_{R\uparrow,ij}^>/<(E) = i \int \frac{d\omega}{2\pi} G_{\downarrow,ij}^>/<(E - \hbar\omega) \Sigma_{R,ij}^>/<(\omega), \quad (7)$$

$$\bar{\Sigma}_{R\downarrow,ij}^>/<(E) = i \int \frac{d\omega}{2\pi} G_{\uparrow,ij}^>/<(E + \hbar\omega) \Sigma_{R,ji}^</>(\omega), \quad (8)$$

$$\bar{\Sigma}_{R\uparrow,ij}^r(E) = i \int \frac{d\omega}{2\pi} \left[G_{\downarrow,ij}^r(E - \hbar\omega) \Sigma_{R,ij}^<(\omega) + G_{\downarrow,ij}^>(E - \hbar\omega) \Sigma_{R,ij}^r(\omega) \right], \quad (9)$$

$$\bar{\Sigma}_{R\downarrow,ij}^r(E) = i \int \frac{d\omega}{2\pi} \left[G_{\uparrow,ij}^r(E + \hbar\omega) \Sigma_{R,ji}^<(\omega) + G_{\uparrow,ij}^<(E + \hbar\omega) \Sigma_{R,ji}^a(\omega) \right]. \quad (10)$$

Here, the subscripts i and j label the matrix elements. Σ_R is the right-lead self-energy, and its relations to the linewidth function Γ_R are $\Sigma_R^r(\omega) = [\Sigma_R^a(\omega)]^\dagger = -i\Gamma_R(\omega)/2$, $\Sigma_R^>(\omega) = -i[n_R(\omega) + 1]\Gamma_R(\omega)$, and $\Sigma_R^<(\omega) = -in_R(\omega)\Gamma_R(\omega)$ where $n_R(\omega) = 1/[e^{(\hbar\omega)/(k_B T_R)} - 1]$ is the Bose–Einstein distribution. In the presence of phonon chirality, phonon branches with opposite circular polarizations exhibit nondegenerate dispersions. Under a thermal bias, the resulting imbalance in their occupations can give rise to a net phonon angular momentum current. By contrast, in the nonchiral limit, the angular-momentum contributions from modes with opposite circular polarizations cancel. Since the present model does not microscopically resolve the individual chiral branches, we

represent the net chiral-phonon contribution of the right reservoir by a super-Ohmic spectral density [66–68]

$$J_R(\omega) = \alpha \hbar \frac{\omega^3}{\omega_0^2} e^{-\omega/\omega_0}, \quad (11)$$

where the dimensionless parameter α describes the dissipation into the reservoir and $\hbar\omega_0$ is the cutoff energy. The spectral density J_R describes the coupling strength between the phonons with energy $\hbar\omega$ in the right reservoir and the electrons in the central region. Using this spectral density, the right-lead linewidth function is taken to be $\Gamma_R(\omega) = J_R(\omega)\mathbf{I}$.

Because the net charge current vanishes, $I_\uparrow^e + I_\downarrow^e = 0$, and thus $I_\uparrow^e = -I_\downarrow^e$. For simplicity, we focus on the spin-up contribution, i.e., $I_s = (\hbar/e)I_\uparrow^e$. Using Eq. (5), we obtain the expression for the spin current

$$I_s = \int \frac{dE}{2\pi} \text{Tr} \left\{ \mathbf{G}_\uparrow^r \left[i f_L \bar{\Sigma}_{R\uparrow}^> + i(1 - f_L) \bar{\Sigma}_{R\uparrow}^< \right] \mathbf{G}_\uparrow^a \Gamma_{L\uparrow} \right\}. \quad (12)$$

The Green's functions in Eqs. (5) and (6), together with the phonon self-energies in Eqs. (7)–(10), form a closed set of equations and are solved self-consistently until convergence is reached. The left-lead spin current I_s is then calculated using Eq. (12). In this Letter, we focus only on the spin current in the left lead. In the Supplemental Material, we derive the expression for the pAM current in the right lead and verify the current conservation [65].

Negative differential SSE—We consider a two-terminal setup to simulate the SSE in the NM-CI system, as shown in Fig. 1(b). T_L and T_R denote the temperatures of the left and right leads, respectively. Thus the thermal bias is $\Delta T = T_L - T_R$. We further define $T_0 = (T_L + T_R)/2$ and then $T_L = T_0 + \Delta T/2$ and $T_R = T_0 - \Delta T/2$. The chemical potential of the left lead μ_L is tunable, whereas we set $\mu_R = 0$. We introduce a shift ε_d of the interfacial on-site potential to examine its influence on spin transport. The phenomena discussed in this work do not qualitatively depend on the dimensionality of the system. Numerical tests show that the spin current is independent of the central-region length along the transport direction. Therefore, for simplicity, the central region is modeled as a quantum dot, whose Hamiltonian is given by $H_{\text{dot}} = 2t \sum_\sigma c_\sigma^\dagger c_\sigma$ with $t = 21.768$ meV. We also present the spin-current results for different central-region sizes in the Supplemental Material [65].

We first study the dependence of the spin current I_s on the thermal bias ΔT at different average temperatures T_0 , with $\mu_L = 1$ meV and $\varepsilon_d = 0$, as shown in Fig. 2(a). For $\Delta T > 0$, the spin current I_s increases monotonically with ΔT . In addition, the overall magnitude of I_s increases as T_0 increases. For $\Delta T < 0$, the magnitude $|I_s|$ initially increases with $|\Delta T|$, but begins to decrease once $|\Delta T|$ exceeds a critical value. This counterintuitive regime, in which the magnitude of the spin current decreases as the magnitude of the thermal bias increases, is

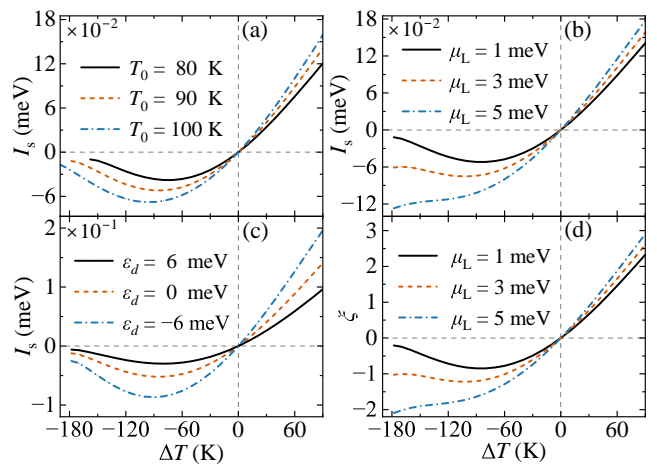


FIG. 2. Spin current I_s as a function of the thermal bias ΔT (a) for different T_0 with $\mu_L = 1$ meV and $\varepsilon_d = 0$, (b) for different μ_L with $T_0 = 90$ K and $\varepsilon_d = 0$, and (c) for different ε_d with $\mu_L = 1$ meV and $T_0 = 90$ K. (d) ξ plotted as a function of ΔT for different μ_L with $T_0 = 90$ K and $\varepsilon_d = 0$. The other parameters are $\alpha = 5$ and $\hbar\omega_0 = 7$ meV.

referred to as the negative differential SSE. Negative differential SSE has been reported in phonon thermal transport [69] and magnon spin transport [70]. Here we show that this phenomenon can also occur in the NM-CI heterostructure.

The negative differential SSE can be explained in terms of the competition between the thermal bias and the left-lead electron density. For $\Delta T > 0$, increasing ΔT —that is, raising T_L and lowering T_R —increases the population of thermally excited electrons in the left lead and promotes spin-phonon conversion at the interface, thereby enhancing the spin current. Consequently, I_s increases monotonically as ΔT increases. For $\Delta T < 0$, increasing $|\Delta T|$ enhances the thermal driving experienced by electrons in the central region. Meanwhile, in this process, T_L decreases and the thermal excitation of electrons is suppressed, which weakens the spin-phonon conversion and reduces the spin current. Thus the competition between these two effects gives rise to negative differential SSE at lower T_L .

We further examine the influence of the left-lead chemical potential μ_L on the spin transport, as shown in Fig. 2(b). For $\mu_L = 1$ meV, the spin current still exhibits pronounced negative differential SSE. As μ_L increases, the negative differential effect becomes less pronounced at $\mu_L = 3$ meV and eventually disappears at $\mu_L = 5$ meV. Since the decrease in thermally excited electron density due to lowering T_L is compensated by the increase in electron density caused by raising the chemical potential, the negative differential SSE disappears for a higher chemical potential.

As demonstrated in studies of the magnon-mediated SSE [71–73], inserting a thin NiO or MoS₂ layer at the

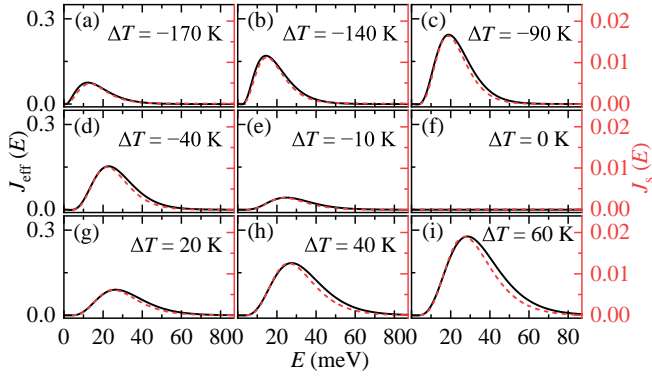


FIG. 3. Effective spectral density $J_{\text{eff}}(E)$ and spin current density $J_s(E)$ as a function of energy E at different ΔT for $\mu_L = 1$ meV. Other parameters: $T_0 = 90$ K, $\varepsilon_d = 0$, $\alpha = 5$, and $\hbar\omega_0 = 7$ meV.

YIG–Pt interface can significantly enhance the spin current. Motivated by these experiments, we examine one possible electronic consequence of an atomically thin interfacial modification by shifting the on-site potential of the lattice site adjacent to the right reservoir, $2t \rightarrow 2t + \varepsilon_d$. This level shift is motivated by the interface-dipole mechanism demonstrated experimentally in Ref. [74], in which a charged atomic-scale interlayer and its compensating screening charge generate an electrostatic potential step. Figure 2(c) presents I_s for different ε_d at $T_0 = 90$ K and $\mu_L = 1$ meV. The spin current increases (decreases) for $\varepsilon_d < 0$ ($\varepsilon_d > 0$), demonstrating that a shift of the interfacial on-site potential can effectively tune spin transport in the NM–CI heterostructure. In the present calculation, we isolate the influence of an interfacial on-site potential shift on spin transport, while the hopping amplitudes, electron-phonon coupling, and phonon spectral density are held fixed. Figure 2(c) should therefore be interpreted as a one-parameter sensitivity analysis rather than as a complete microscopic description of an inserted layer. This approximation is most appropriate for an atomically thin interlayer whose induced electrostatic perturbation is localized within the interfacial region [75]. For a thicker interlayer, an explicit interlayer Hamiltonian together with modified hopping parameters would be required.

By comparing the spin-current expression in Eq. (12) with the Landauer–Büttiker formula [76], we can define the effective spectral density J_{eff} as [77]

$$J_{\text{eff}}(E) = \text{Tr} \left\{ i f_L(E) \bar{\Sigma}_{R\uparrow}^>(E) + i [1 - f_L(E)] \bar{\Sigma}_{R\uparrow}^<(E) \right\}. \quad (13)$$

The effective spectral density J_{eff} can be interpreted as the effective coupling strength between the NM and the CI. This interpretation follows from the fact that the phonon self-energy in J_{eff} is written in the simplified form $\bar{\Sigma} \sim G \Sigma_R$, which represents the coupling between the central region and the right lead. Accordingly, we define

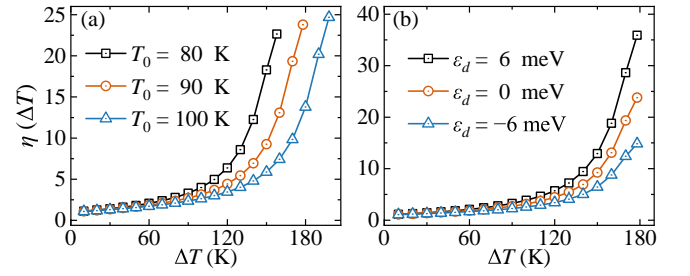


FIG. 4. (a) Rectification ratio η as a function of ΔT for different T_0 with $\mu_L = 1$ meV and $\varepsilon_d = 0$. (b) η as a function of ΔT for different ε_d with $T_0 = 90$ K and $\mu_L = 1$ meV.

ξ as

$$\xi = \int J_{\text{eff}}(E) dE, \quad (14)$$

which represents the overall contribution of the effective interfacial coupling. Below, we show that the spin-transport behavior is closely related to ξ and J_{eff} .

Figure 2(d) shows ξ as a function of ΔT for different μ_L at $T_0 = 90$ K and $\varepsilon_d = 0$. A comparison with I_s in Fig. 2(b) reveals a strong correlation between the spin current and ξ . To elucidate the spin transport properties in detail, we plot the effective spectral density J_{eff} and the spin-current spectrum J_s at different values of ΔT for $\mu_L = 1$ meV, as shown in Fig. 3. The spin-current spectrum J_s is defined as the integrand in Eq. (12). As ΔT decreases from 0 to -170 K, equivalently as $|\Delta T|$ increases, both J_{eff} and J_s initially increase [Figs. 3(c)–3(f)], reach their maxima at $\Delta T = -90$ K [Fig. 3(c)], and then decrease [Figs. 3(a)–3(c)]. This trend is fully consistent with the variation of I_s in Fig. 2(b) for $\mu_L = 1$ meV. Thus, as shown in Figs. 2(d) and 3, the strong correlations between ξ and I_s , and between J_{eff} and J_s , illustrate the crucial role of the effective interfacial spectral density in determining the spin-transport behavior in the NM–CI heterostructure.

Rectification effect and thermal spin diode—As shown in Fig. 2, in addition to the negative differential SSE discussed above, the spin current also exhibits rectification; that is, its magnitude is asymmetric under reversal of the thermal bias: $|I_s(\Delta T)| \neq |I_s(-\Delta T)|$. The spin-current asymmetry stems from the structural asymmetry between the left and right leads, and the resulting nonreciprocal spin transport can be used to realize a thermally controlled spin diode effect [78]. We can define a rectification ratio η to quantify the rectification performance of the spin diode as

$$\eta(\Delta T) = \left| \frac{I_s(\Delta T)}{I_s(-\Delta T)} \right|, \quad \Delta T > 0. \quad (15)$$

The ratio is widely used to quantify the performance of thermal [69, 79], electronic [80, 81], and spin diodes [82].

Figure 4(a) presents the rectification ratio for different T_0 at $\mu_L = 1$ meV and $\varepsilon_d = 0$. The rectification ratio increases with the thermal bias ΔT and reaches a maximum value of approximately 25. Figure 4(b) shows the rectification ratio for different ε_d at $T_0 = 90$ K and $\mu_L = 1$ meV. The results show that η can be enhanced (diminished) for $\varepsilon_d > 0$ ($\varepsilon_d < 0$), demonstrating that the interfacial on-site potential provides an effective means to tune the performance of the thermal spin diode.

Conclusion—In summary, we investigate the nonlinear spin-transport properties of the chiral-phonon-mediated spin Seebeck effect. We consider a two-terminal NM–CI setup and develop a framework for calculating the spin current within the nonequilibrium Green’s function formalism. We discuss the influence of (i) the temperature difference between the NM and the CI, (ii) the chemical potential of the NM, and (iii) the modification of the interfacial on-site potential on the spin transport properties. We identify two characteristic nonlinear spin-transport phenomena: negative differential SSE and spin-current rectification. The negative differential effect arises from the competition between the thermal bias and the thermally excited electron density, and the rectification effect originates from the structural asymmetry of the two-terminal setup. The spin-transport behavior is closely related to an effective interfacial spectral density J_{eff} and its energy integral ξ . Furthermore, we suggest that spin-current rectification can be exploited to realize a thermal spin diode. We calculate the corresponding rectification ratio η to characterize the diode efficiency. This work provides a novel approach to realizing thermally controlled spintronic devices using chiral phonons.

Acknowledgments—J.Z. and Y.X. are supported by the National Natural Science Foundation of China (Grant No. 12174023). G.L. is supported by the Youth Innovation Team of Shaanxi Universities (Grant No. 25JP021). G.T. is supported by the National Natural Science Foundation of China (Grants No. 12088101 and No. 12374048).

* gmtang@gscaep.ac.cn

† xingyanxia@bit.edu.cn

- [1] I. Žutić, J. Fabian, and S. Das Sarma, Spintronics: Fundamentals and applications, *Rev. Mod. Phys.* **76**, 323 (2004).
- [2] S. Bader and S. Parkin, Spintronics, *Annu. Rev. Condens. Matter Phys.* **1**, 71 (2010).
- [3] S. Bandyopadhyay and M. Cahay, *Introduction to spintronics* (CRC press, 2008).
- [4] Y. Kajiwara, K. Harii, S. Takahashi, J.-i. Ohe, K. Uchida, M. Mizuguchi, H. Umezawa, H. Kawai, K. Ando, K. Takanashi, *et al.*, Transmission of electrical signals by spin-wave interconversion in a magnetic insulator, *Nature* **464**, 262 (2010).
- [5] L. J. Cornelissen, J. Liu, R. A. Duine, J. B. Youssef, and B. J. van Wees, Long-distance transport of magnon spin information in a magnetic insulator at room temperature, *Nat. Phys.* **11**, 1022 (2015).
- [6] B. Heinrich, C. Burrowes, E. Montoya, B. Kardasz, E. Girt, Y.-Y. Song, Y. Sun, and M. Wu, Spin Pumping at the Magnetic Insulator (YIG)/Normal Metal (Au) Interfaces, *Phys. Rev. Lett.* **107**, 066604 (2011).
- [7] M. Matsuo, Y. Ohnuma, T. Kato, and S. Maekawa, Spin Current Noise of the Spin Seebeck Effect and Spin Pumping, *Phys. Rev. Lett.* **120**, 037201 (2018).
- [8] Y. Ominato, M. Yama, A. Yamakage, M. Matsuo, and T. Kato, Spin pumping into two-dimensional systems, *J. Phys.: Condens. Matter* **37**, 433001 (2025).
- [9] H. Adachi, K.-i. Uchida, E. Saitoh, and S. Maekawa, Theory of the spin Seebeck effect, *Rep. Prog. Phys.* **76**, 036501 (2013).
- [10] K. Uchida, S. Takahashi, K. Harii, J. Ieda, W. Koshibae, K. Ando, S. Maekawa, and E. Saitoh, Observation of the spin Seebeck effect, *Nature* **455**, 778 (2008).
- [11] K. Uchida, S. Takahashi, J. Ieda, K. Harii, K. Ikeda, W. Koshibae, S. Maekawa, and E. Saitoh, Phenomenological analysis for spin-Seebeck effect in metallic magnets, *J. Appl. Phys.* **105**, 07C908 (2009).
- [12] K. Uchida, J. Xiao, H. Adachi, J. Ohe, S. Takahashi, J. Ieda, T. Ota, Y. Kajiwara, H. Umezawa, H. Kawai, G. E. W. Bauer, S. Maekawa, and E. Saitoh, Spin Seebeck insulator, *Nat. Mater.* **9**, 894 (2010).
- [13] E. Saitoh, M. Ueda, H. Miyajima, and G. Tatara, Conversion of spin current into charge current at room temperature: Inverse spin-Hall effect, *Appl. Phys. Lett.* **88**, 182509 (2006).
- [14] S. O. Valenzuela and M. Tinkham, Direct electronic measurement of the spin Hall effect, *Nature* **442**, 176 (2006).
- [15] T. Kimura, Y. Otani, T. Sato, S. Takahashi, and S. Maekawa, Room-Temperature Reversible Spin Hall Effect, *Phys. Rev. Lett.* **98**, 156601 (2007).
- [16] F. Mahfouzi and B. K. Nikolić, Signatures of electron-magnon interaction in charge and spin currents through magnetic tunnel junctions: A nonequilibrium many-body perturbation theory approach, *Phys. Rev. B* **90**, 045115 (2014).
- [17] G. Li, H. Jin, Y. Wei, and J. Wang, Giant effective electron-magnon coupling in a nonmagnetic metal–ferromagnetic insulator heterostructure, *Phys. Rev. B* **106**, 205303 (2022).
- [18] G. Li and J. Wang, Spin transport study in a disordered-metal/ferromagnetic-insulator heterostructure based on full counting statistics within the coherent potential approximation, *Phys. Rev. B* **109**, 125403 (2024).
- [19] G. Tang, X. Chen, J. Ren, and J. Wang, Rectifying full-counting statistics in a spin Seebeck engine, *Phys. Rev. B* **97**, 081407 (2018).
- [20] J. Zheng, S. Bender, J. Armaitis, R. E. Troncoso, and R. A. Duine, Green’s function formalism for spin transport in metal-insulator-metal heterostructures, *Phys. Rev. B* **96**, 174422 (2017).
- [21] Y. H. Shen, X. S. Wang, and X. R. Wang, Thermal spin current and spin accumulation at ferromagnetic insulator/nonmagnetic metal interface, *Phys. Rev. B* **94**, 014403 (2016).
- [22] T. Kato, Y. Ohnuma, M. Matsuo, J. Rech, T. Jonckheere, and T. Martin, Microscopic theory of spin transport at the interface between a superconductor and a ferromagnetic insulator, *Phys. Rev. B* **99**, 144411 (2019).

- [23] L. G. Johnsen, H. T. Simensen, A. Brataas, and J. Linder, Magnon Spin Current Induced by Triplet Cooper Pair Supercurrents, *Phys. Rev. Lett.* **127**, 207001 (2021).
- [24] M. A. Silaev, Finite-frequency spin susceptibility and spin pumping in superconductors with spin-orbit relaxation, *Phys. Rev. B* **102**, 144521 (2020).
- [25] S. Seki, T. Ideue, M. Kubota, Y. Kozuka, R. Takagi, M. Nakamura, Y. Kaneko, M. Kawasaki, and Y. Tokura, Thermal Generation of Spin Current in an Antiferromagnet, *Phys. Rev. Lett.* **115**, 266601 (2015).
- [26] S. M. Rezende, R. L. Rodríguez-Suárez, and A. Azevedo, Theory of the spin Seebeck effect in antiferromagnets, *Phys. Rev. B* **93**, 014425 (2016).
- [27] Y. Ohnuma, H. Adachi, E. Saitoh, and S. Maekawa, Spin Seebeck effect in antiferromagnets and compensated ferrimagnets, *Phys. Rev. B* **87**, 014423 (2013).
- [28] Q. Cui, B. Zeng, P. Cui, T. Yu, and H. Yang, Efficient spin Seebeck and spin Nernst effects of magnons in altermagnets, *Phys. Rev. B* **108**, L180401 (2023).
- [29] E. W. Hodt and J. Linder, Spin pumping in an altermagnet/normal-metal bilayer, *Phys. Rev. B* **109**, 174438 (2024).
- [30] C. Sun and J. Linder, Spin pumping from a ferromagnetic insulator into an altermagnet, *Phys. Rev. B* **108**, L140408 (2023).
- [31] J. Bardeen, L. N. Cooper, and J. R. Schrieffer, Theory of Superconductivity, *Phys. Rev.* **108**, 1175 (1957).
- [32] N. Li, J. Ren, L. Wang, G. Zhang, P. Hänggi, and B. Li, Colloquium: Phononics: Manipulating heat flow with electronic analogs and beyond, *Rev. Mod. Phys.* **84**, 1045 (2012).
- [33] T. Yamamoto and K. Watanabe, Nonequilibrium Green's Function Approach to Phonon Transport in Defective Carbon Nanotubes, *Phys. Rev. Lett.* **96**, 255503 (2006).
- [34] J.-S. Wang, J. Wang, and N. Zeng, Nonequilibrium Green's function approach to mesoscopic thermal transport, *Phys. Rev. B* **74**, 033408 (2006).
- [35] C. Strohm, G. L. J. A. Rikken, and P. Wyder, Phenomenological Evidence for the Phonon Hall Effect, *Phys. Rev. Lett.* **95**, 155901 (2005).
- [36] L. Sheng, D. N. Sheng, and C. S. Ting, Theory of the Phonon Hall Effect in Paramagnetic Dielectrics, *Phys. Rev. Lett.* **96**, 155901 (2006).
- [37] S. Dai, Z. Fei, Q. Ma, A. S. Rodin, M. Wagner, A. S. McLeod, M. K. Liu, W. Gannett, W. Regan, K. Watanabe, T. Taniguchi, M. Thiemens, G. Dominguez, A. H. C. Neto, A. Zettl, F. Keilmann, P. Jarillo-Herrero, M. M. Fogler, and D. N. Basov, Tunable Phonon Polaritons in Atomically Thin van der Waals Crystals of Boron Nitride, *Science* **343**, 1125 (2014).
- [38] X. G. Xu, B. G. Ghamsari, J.-H. Jiang, L. Gilburd, G. O. Andreev, C. Zhi, Y. Bando, D. Golberg, P. Berini, and G. C. Walker, One-dimensional surface phonon polaritons in boron nitride nanotubes, *Nat. Commun.* **5**, 4782 (2014).
- [39] N. Rivera, T. Christensen, and P. Narang, Phonon Polaritons in Two-Dimensional Materials, *Nano Lett.* **19**, 2653 (2019).
- [40] L. Zhang and Q. Niu, Angular Momentum of Phonons and the Einstein-de Haas Effect, *Phys. Rev. Lett.* **112**, 085503 (2014).
- [41] L. Zhang and Q. Niu, Chiral Phonons at High-Symmetry Points in Monolayer Hexagonal Lattices, *Phys. Rev. Lett.* **115**, 115502 (2015).
- [42] H. Ueda, M. García-Fernández, S. Agrestini, C. P. Romao, J. van den Brink, N. A. Spaldin, K.-J. Zhou, and U. Staub, Chiral phonons in quartz probed by X-rays, *Nature* **618**, 946 (2023).
- [43] H. Zhang, N. Peshcherenko, F. Yang, T. Z. Ward, P. Raghuvanshi, L. Lindsay, C. Felser, Y. Zhang, J.-Q. Yan, and H. Miao, Measurement of phonon angular momentum, *Nat. Phys.* **21**, 1387 (2025).
- [44] H. Zhu, J. Yi, M.-Y. Li, J. Xiao, L. Zhang, C.-W. Yang, R. A. Kaindl, L.-J. Li, Y. Wang, and X. Zhang, Observation of chiral phonons, *Science* **359**, 579 (2018).
- [45] K. Ishito, H. Mao, Y. Kousaka, Y. Togawa, S. Iwasaki, T. Zhang, S. Murakami, J.-i. Kishine, and T. Satoh, Truly chiral phonons in α -HgS, *Nat. Phys.* **19**, 35 (2023).
- [46] D. M. Juraschek, R. M. Geilhufe, H. Zhu, M. Basini, P. Baum, A. Baydin, S. Chaudhary, M. Fechner, B. Flebus, G. Grissonnanche, A. I. Kirilyuk, M. Leshchko, S. F. Maehrlein, M. Mignolet, S. Murakami, Q. Niu, U. Nowak, C. P. Romao, H. Rostami, T. Satoh, N. A. Spaldin, H. Ueda, and L. Zhang, Chiral phonons, *Nat. Phys.* **21**, 1532 (2025).
- [47] D. M. Juraschek and N. A. Spaldin, Orbital magnetic moments of phonons, *Phys. Rev. Mater.* **3**, 064405 (2019).
- [48] J. Kishine, A. S. Ovchinnikov, and A. A. Tereshchenko, Chirality-Induced Phonon Dispersion in a Noncentrosymmetric Micropolar Crystal, *Phys. Rev. Lett.* **125**, 245302 (2020).
- [49] M. Che, J. Liang, Y. Cui, H. Li, B. Lu, W. Sang, X. Li, X. Dong, L. Zhao, S. Zhang, T. Sun, W. Jiang, E. Liu, F. Jin, T. Zhang, and L. Yang, Magnetic Order Induced Chiral Phonons in a Ferromagnetic Weyl Semimetal, *Phys. Rev. Lett.* **134**, 196906 (2025).
- [50] K. Ishito, H. Mao, K. Kobayashi, Y. Kousaka, Y. Togawa, H. Kusunose, J.-i. Kishine, and T. Satoh, Chiral phonons: circularly polarized Raman spectroscopy and ab initio calculations in a chiral crystal tellurium, *Chirality* **35**, 338 (2023).
- [51] K. Ohe, H. Shishido, M. Kato, S. Utsumi, H. Matsuura, and Y. Togawa, Chirality-Induced Selectivity of Phonon Angular Momenta in Chiral Quartz Crystals, *Phys. Rev. Lett.* **132**, 056302 (2024).
- [52] T. Yokoyama, Phonon Edelstein effect in chiral metals, *Phys. Rev. B* **112**, L020406 (2025).
- [53] X. Qin, C. Yang, D. Sun, J. Liu, and V. Blum, Chiral Phonon-Induced Spin Transport via Microscopic Barnett Effect, *Phys. Rev. Lett.* **135**, 076703 (2025).
- [54] H. Chen, W. Wu, J. Zhu, Z. Yang, W. Gong, W. Gao, S. A. Yang, and L. Zhang, Chiral Phonon Diode Effect in Chiral Crystals, *Nano Lett.* **22**, 1688 (2022).
- [55] Y. Nabei, C. Yang, H. Sun, H. Jones, T. Mai, T. Wang, R. Bodin, B. Pandey, Z. Wang, Y. Xiong, A. H. Comstock, B. Ewing, J. Bingen, R. Sun, D. Smirnov, W. Zhang, A. Hoffmann, R. Rao, M. Hu, Z. V. Vardeny, B. Yan, X. Li, J. Zhou, J. Liu, and D. Sun, Orbital Seebeck effect induced by chiral phonons, *Nat. Phys.* **22**, 245 (2026).
- [56] K. Kim, E. Vetter, L. Yan, C. Yang, Z. Wang, R. Sun, Y. Yang, A. H. Comstock, X. Li, J. Zhou, L. Zhang, W. You, D. Sun, and J. Liu, Chiral-phonon-activated spin Seebeck effect, *Nat. Mater.* **22**, 322 (2023).
- [57] T. Funato, M. Matsuo, and T. Kato, Chirality-Induced Phonon-Spin Conversion at an Interface, *Phys. Rev. Lett.* **132**, 236201 (2024).
- [58] N. Nishimura, T. Funato, M. Matsuo, and T. Kato, The-

- ory of spin Seebeck effect activated by acoustic chiral phonons, *J. Magn. Magn. Mater.* **630**, 173386 (2025).
- [59] H. Haug and A.-P. Jauho, *Quantum kinetics in transport and optics of semiconductors* (Springer, 2008).
- [60] G. Stefanucci and R. van Leeuwen, *Nonequilibrium Many-Body Theory of Quantum Systems: A Modern Introduction*, 2nd ed. (Cambridge University Press, 2025).
- [61] R. A. Jishi, *Feynman Diagram Techniques in Condensed Matter Physics* (Cambridge University Press, 2013).
- [62] Y. Meir and N. S. Wingreen, Landauer formula for the current through an interacting electron region, *Phys. Rev. Lett.* **68**, 2512 (1992).
- [63] M. P. L. Sancho, J. M. L. Sancho, and J. Rubio, Quick iterative scheme for the calculation of transfer matrices: application to Mo (100), *J. Phys. F: Met. Phys.* **14**, 1205 (1984).
- [64] M. P. L. Sancho, J. M. L. Sancho, and J. Rubio, Highly convergent schemes for the calculation of bulk and surface Green functions, *J. Phys. F: Met. Phys.* **15**, 851 (1985).
- [65] See Supplemental Material at [to be inserted] for derivations of the left-lead spin-current expression and the central-region Green's functions, the expression for the right-lead phonon-angular-momentum current, verification of current conservation, the lattice Hamiltonian of the normal metal, and spin-current results for systems of different dimensionalities; the Supplemental Material includes Refs. [57, 59, 63, 64, 66–68].
- [66] U. Weiss, *Quantum Dissipative Systems* (World Scientific, 2008).
- [67] M. Thorwart, J. Eckel, and E. R. Mucciolo, Non-Markovian dynamics of double quantum dot charge qubits due to acoustic phonons, *Phys. Rev. B* **72**, 235320 (2005).
- [68] Q.-S. Tan, W. Wu, L. Xu, J. Liu, and L.-M. Kuang, Quantum sensing of supersensitivity for the Ohmic quantum reservoir, *Phys. Rev. A* **106**, 032602 (2022).
- [69] B. Li, L. Wang, and G. Casati, Thermal Diode: Rectification of Heat Flux, *Phys. Rev. Lett.* **93**, 184301 (2004).
- [70] J. Ren, Predicted rectification and negative differential spin Seebeck effect at magnetic interfaces, *Phys. Rev. B* **88**, 220406 (2013).
- [71] H. Wang, C. Du, P. C. Hammel, and F. Yang, Antiferromagnonic Spin Transport from $\text{Y}_3\text{Fe}_5\text{O}_{12}$ into NiO, *Phys. Rev. Lett.* **113**, 097202 (2014).
- [72] W. Lin, K. Chen, S. Zhang, and C. L. Chien, Enhancement of Thermally Injected Spin Current through an Antiferromagnetic Insulator, *Phys. Rev. Lett.* **116**, 186601 (2016).
- [73] W.-Y. Lee, N.-W. Park, G.-S. Kim, M.-S. Kang, J. W. Choi, K.-Y. Choi, H. W. Jang, E. Saitoh, and S.-K. Lee, Enhanced Spin Seebeck Thermopower in Pt/Holey $\text{MoS}_2/\text{Y}_3\text{Fe}_5\text{O}_{12}$ Hybrid Structure, *Nano Lett.* **21**, 189 (2021).
- [74] T. Yajima, Y. Hikita, M. Minohara, C. Bell, J. A. Mundy, L. F. Kourkoutis, D. A. Muller, H. Kumigashira, M. Oshima, and H. Y. Hwang, Controlling band alignments by artificial interface dipoles at perovskite heterointerfaces, *Nat. Commun.* **6**, 6759 (2015).
- [75] R. T. Tung, Formation of an electric dipole at metal-semiconductor interfaces, *Phys. Rev. B* **64**, 205310 (2001).
- [76] S. Datta, *Electronic Transport in Mesoscopic Systems* (Cambridge University Press, 1995).
- [77] N. Sergueev, Q.-f. Sun, H. Guo, B. G. Wang, and J. Wang, Spin-polarized transport through a quantum dot: Anderson model with on-site Coulomb repulsion, *Phys. Rev. B* **65**, 165303 (2002).
- [78] J. Ren and J.-X. Zhu, Theory of asymmetric and negative differential magnon tunneling under temperature bias: Towards a spin Seebeck diode and transistor, *Phys. Rev. B* **88**, 094427 (2013).
- [79] J. Ren and J.-X. Zhu, Heat diode effect and negative differential thermal conductance across nanoscale metal-dielectric interfaces, *Phys. Rev. B* **87**, 241412 (2013).
- [80] R. Cheng, D. Li, H. Zhou, C. Wang, A. Yin, S. Jiang, Y. Liu, Y. Chen, Y. Huang, and X. Duan, Electroluminescence and Photocurrent Generation from Atomically Sharp $\text{WSe}_2/\text{MoS}_2$ Heterojunction p - n Diodes, *Nano Lett.* **14**, 5590 (2014).
- [81] Z. Li, K. Yuan, and Y. Ye, High rectification ratio metal-insulator-semiconductor tunnel diode based on single-layer MoS_2 , *Nanotechnology* **31**, 075202 (2019).
- [82] A. Iovan, S. Andersson, Y. G. Naidyuk, A. Vedyayev, B. Dieny, and V. Korenivski, Spin Diode Based on Fe/MgO Double Tunnel Junction, *Nano Lett.* **8**, 805 (2008).

Supplementary Materials for “Spin Seebeck Effect in Normal-Metal–Chiral-Insulator Heterostructure”

Jiayan Zhang,¹ Gaoyang Li,² Gaomin Tang,^{3,*} and Yanxia Xing^{1,†}

¹*Key Laboratory of Advanced Optoelectronic Quantum Architecture and Measurement, Ministry of Education, Beijing Institute of Technology, Beijing 100081, China*

²*School of Physics & Information Science, Shaanxi University of Science & Technology, Xi'an 710021, China*

³*Graduate School of China Academy of Engineering Physics, Beijing 100193, China*

CONTENTS

S1. The expression of the spin current in the left lead	1
S2. The Green's function of the central region	2
S3. The expression of the phonon angular momentum current in the right lead	5
S4. Verification of current conservation	6
S5. The lattice Hamiltonian of the normal metal	6
S6. The spin current for different central-region sizes and dimensionalities	7
References	7

S1. THE EXPRESSION OF THE SPIN CURRENT IN THE LEFT LEAD

In this section, we present the expression for the spin current in the left lead, defined as

$$I_s = \frac{\hbar}{2e} (I_{\uparrow}^e - I_{\downarrow}^e), \quad (\text{S1})$$

where I_{σ}^e is the spin-dependent charge current in the left lead. From the spin-dependent electron-number operator in the left lead, $\mathcal{N}_{L\sigma} = \sum_{\mathbf{k}} b_{\mathbf{k}\sigma}^{\dagger} b_{\mathbf{k}\sigma}$, the charge current is

$$\begin{aligned} I_{\sigma}^e(t) &= -e \left\langle \frac{d}{dt} \mathcal{N}_{L\sigma} \right\rangle = -\frac{ie}{\hbar} \langle [\mathcal{H}, \mathcal{N}_{L\sigma}] \rangle \\ &= -\frac{ie}{\hbar} \sum_{n\mathbf{k}} \left[t_{n\mathbf{k}\sigma} \langle c_{n\sigma}^{\dagger}(t) b_{\mathbf{k}\sigma}(t) \rangle - t_{n\mathbf{k}\sigma}^* \langle b_{\mathbf{k}\sigma}^{\dagger}(t) c_{n\sigma}(t) \rangle \right]. \end{aligned} \quad (\text{S2})$$

We define the lesser mixed Green's functions between the left lead (L) and the central region (C) by

$$G_{\sigma,\mathbf{k}n}^{\leq}(t, t') = \frac{i}{\hbar} \langle c_{n\sigma}^{\dagger}(t') b_{\mathbf{k}\sigma}(t) \rangle, \quad G_{\sigma,n\mathbf{k}}^{\leq}(t, t') = \frac{i}{\hbar} \langle b_{\mathbf{k}\sigma}^{\dagger}(t') c_{n\sigma}(t) \rangle, \quad (\text{S3})$$

We have $G_{\sigma,\mathbf{k}n}^{\leq}(t, t') = -[G_{\sigma,n\mathbf{k}}^{\leq}(t', t)]^{\dagger}$. Then the spin-dependent electric current can be expressed as

$$I_{\sigma}^e(t) = -e \sum_{n\mathbf{k}} t_{n\mathbf{k}\sigma} [G_{\sigma,\mathbf{k}n}^{\leq}(t, t) + \text{h.c.}]. \quad (\text{S4})$$

To obtain $G_{\sigma,\mathbf{k}n}^{\leq}(t, t)$, we first define the contour-ordered Green's function as

$$G_{\sigma,\mathbf{k}n}(\tau, \tau') = -\frac{i}{\hbar} \langle \mathcal{T}_c b_{\mathbf{k}\sigma}(\tau) c_{n\sigma}^{\dagger}(\tau') \rangle = -\frac{i}{\hbar} \langle \mathcal{T}_c \mathcal{S} b_{\mathbf{k}\sigma}(\tau) c_{n\sigma}^{\dagger}(\tau') \rangle_0. \quad (\text{S5})$$

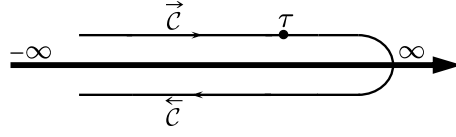


FIG. S1. Keldysh contour. The contour runs from $t = -\infty$ to $t = \infty$ along the forward branch $\vec{\mathcal{C}}$, and returns from $t = \infty$ to $t = -\infty$ along the backward branch $\overleftarrow{\mathcal{C}}$.

Here τ and τ' are the variables on the Keldysh contour [see Fig. S1] and \mathcal{T}_c is the contour-ordering operator. $\langle \dots \rangle$ denotes the ensemble average taken with respect to the coupled L-C system, while $\langle \dots \rangle_0$ is taken with respect to the decoupled L-C system in which the left lead and the central region are each in their own thermal equilibrium. The \mathcal{S} -matrix is defined as

$$\mathcal{S} = \mathcal{T}_c \exp \left[-\frac{i}{\hbar} \int_c d\tau \mathcal{H}_T(\tau) \right] = \sum_{n=0}^{\infty} \left(-\frac{i}{\hbar} \right)^n \frac{1}{n!} \int_c d\tau_1 \cdots \int_c d\tau_n \mathcal{T}_c [\mathcal{H}_T(\tau_1) \cdots \mathcal{H}_T(\tau_n)]. \quad (\text{S6})$$

Since expectation values containing an odd number of fermion operators vanish, we retain only even orders in $t_{n\mathbf{k}\sigma}$ in the expansion of $G_{\sigma,\mathbf{k}n}(\tau, \tau')$. At zeroth order, $G_{\sigma,\mathbf{k}n}^{(0)}(\tau, \tau') = 0$. To second order, we obtain

$$G_{\sigma,\mathbf{k}n}^{(2)}(\tau, \tau') = \sum_m \int_c d\tau_1 [t_{m\mathbf{k}\sigma}^* g_{\mathbf{k}\sigma}(\tau, \tau_1) g_{\sigma,mn}(\tau_1, \tau')], \quad (\text{S7})$$

where we defined the following noninteracting Green's functions of the left lead and the central region

$$g_{\mathbf{k}\sigma}(\tau, \tau_1) = -\frac{i}{\hbar} \langle \mathcal{T}_c b_{\mathbf{k}\sigma}(\tau) b_{\mathbf{k}\sigma}^\dagger(\tau_1) \rangle_0, \quad g_{\sigma,mn}(\tau_1, \tau') = -\frac{i}{\hbar} \langle \mathcal{T}_c c_{m\sigma}(\tau_1) c_{n\sigma}^\dagger(\tau') \rangle_0. \quad (\text{S8})$$

Summing contributions from all higher even orders, the Green's function becomes

$$G_{\sigma,\mathbf{k}n}(\tau, \tau') = \sum_m \int_c d\tau_1 [t_{m\mathbf{k}\sigma}^* g_{\mathbf{k}\sigma}(\tau, \tau_1) G_{\sigma,mn}(\tau_1, \tau')]. \quad (\text{S9})$$

Applying the Langreth rules [1] and taking the Fourier transform, we obtain

$$G_{\sigma,\mathbf{k}n}^<(t-t') = \frac{1}{\hbar} \sum_m \int \frac{dE}{2\pi} [g_{\mathbf{k}\sigma}^r(E) t_{m\mathbf{k}\sigma} G_{\sigma,mn}^<(E) + g_{\mathbf{k}\sigma}^<(E) t_{m\mathbf{k}\sigma} G_{\sigma,mn}^a(E)] e^{-iE(t-t')/\hbar}. \quad (\text{S10})$$

Using

$$G_{\sigma,nm}^{<,*}(E) = -G_{\sigma,mn}^<(E), \quad G_{\sigma,nm}^{a,*}(E) = G_{\sigma,mn}^r(E), \quad (\text{S11})$$

and defining the retarded (r), advanced (a) and lesser ($<$) self-energies of the left lead

$$\Sigma_{L\sigma,mn}^{r/a/<}(E) = \sum_{\mathbf{k}} t_{m\mathbf{k}\sigma} g_{\mathbf{k}\sigma}^{r/a/<}(E) t_{\mathbf{k}n\sigma}, \quad (\text{S12})$$

we obtain the spin-dependent electric current in the left lead

$$I_\sigma^e = \frac{e}{\hbar} \int \frac{dE}{2\pi} \text{Tr} \left[\mathbf{G}_\sigma^>(E) \Sigma_{L\sigma}^<(E) - \mathbf{G}_\sigma^<(E) \Sigma_{L\sigma}^>(E) \right]. \quad (\text{S13})$$

After obtaining the I_σ^e , the spin current is calculated using Eq. (S1).

52. THE GREEN'S FUNCTION OF THE CENTRAL REGION

In this section, we evaluate the central-region Green's function in the presence of the self-energies of left electronic and right phononic leads, treating the electron-phonon coupling perturbatively. Following Ref. [2], the electron-phonon interaction between the central region and the right lead is given by

$$\mathcal{H}_{e\text{-ph}} = - \sum_{mq\lambda} \left(\mathcal{J}_{qm} d_{q\lambda}^\dagger c_{m\downarrow}^\dagger c_{m\uparrow} + \mathcal{J}_{qm}^* d_{q\lambda} c_{m\uparrow}^\dagger c_{m\downarrow} \right), \quad (\text{S14})$$

where $\mathcal{J}_{\mathbf{q}m}$ is the electron-phonon coupling strength, and $d_{\mathbf{q}\lambda}^\dagger$ and $d_{\mathbf{q}\lambda}$ are defined as

$$d_{\mathbf{q}\lambda}^\dagger = \eta_{\mathbf{q}\lambda} (a_{\mathbf{q}\lambda} - a_{-\mathbf{q}\bar{\lambda}}^\dagger), \quad d_{\mathbf{q}\lambda} = \eta_{\mathbf{q}\lambda}^* (a_{\mathbf{q}\lambda}^\dagger - a_{-\mathbf{q}\bar{\lambda}}) \quad (\text{S15})$$

where $\eta_{\mathbf{q}\lambda} = \sqrt{\hbar\omega_{\mathbf{q}\lambda}/(2\rho V)}[(\mathbf{q} \times \mathbf{e}_{\mathbf{q}\lambda})_x + i(\mathbf{q} \times \mathbf{e}_{\mathbf{q}\lambda})_y]$. The contour-ordered Green's function for a spin \uparrow electron in the central region is defined as

$$G_{\uparrow,mn}(\tau, \tau') = -\frac{i}{\hbar} \langle \mathcal{T}_c c_{m\uparrow}(\tau) c_{n\uparrow}^\dagger(\tau') \rangle = -\frac{i}{\hbar} \langle \mathcal{T}_c \mathcal{S} c_{m\uparrow}(\tau) c_{n\uparrow}^\dagger(\tau') \rangle_0. \quad (\text{S16})$$

Here \mathcal{T}_c is the contour-ordering operator. The averages $\langle \dots \rangle$ and $\langle \dots \rangle_0$ are taken with respect to the system with and without the electron-phonon interaction, respectively. The \mathcal{S} -matrix is given in Eq. (S6). Since expectation values containing an odd number of operators vanish, we retain only even orders in $\mathcal{J}_{\mathbf{q}m}$. At zeroth order

$$G_{\uparrow,mn}^{(0)}(\tau, \tau') = -\frac{i}{\hbar} \langle \mathcal{T}_c c_{m\uparrow}(\tau) c_{n\uparrow}^\dagger(\tau') \rangle_0. \quad (\text{S17})$$

To second order in $\mathcal{J}_{\mathbf{q}m}$, we obtain

$$G_{\uparrow,mn}^{(2)}(\tau, \tau') = \sum_{n_1 n_2} \iint_c d\tau_1 d\tau_2 \left[g_{\uparrow,mn_1}(\tau, \tau_1) \bar{\Sigma}_{\text{R}\uparrow, n_1 n_2}^0(\tau_1, \tau_2) g_{\uparrow, n_2 n}(\tau_2, \tau') \right], \quad (\text{S18})$$

where we have defined the following noninteracting Green's functions

$$g_{\uparrow, mn_1}(\tau, \tau_1) = -\frac{i}{\hbar} \langle \mathcal{T}_c c_{m\uparrow}(\tau) c_{n_1\uparrow}^\dagger(\tau_1) \rangle_0, \quad g_{\downarrow, n_1 n_2}(\tau_1, \tau_2) = -\frac{i}{\hbar} \langle \mathcal{T}_c c_{n_1\downarrow}(\tau_1) c_{n_2\downarrow}^\dagger(\tau_2) \rangle_0, \quad (\text{S19})$$

$$g_{\mathbf{q}\lambda}(\tau_1, \tau_2) = -\frac{i}{\hbar} \langle \mathcal{T}_c d_{\mathbf{q}\lambda}(\tau_1) d_{\mathbf{q}\lambda}^\dagger(\tau_2) \rangle_0, \quad g_{\uparrow, n_2 n}(\tau_2, \tau') = -\frac{i}{\hbar} \langle \mathcal{T}_c c_{n_2\uparrow}(\tau_2) c_{n\uparrow}^\dagger(\tau') \rangle_0, \quad (\text{S20})$$

and phonon self-energy

$$\bar{\Sigma}_{\text{R}\uparrow, n_1 n_2}^0(\tau_1, \tau_2) = i\hbar \left[g_{\downarrow, n_1 n_2}(\tau_1, \tau_2) \sum_{\mathbf{q}\lambda} \mathcal{J}_{\mathbf{q}n_1}^* g_{\mathbf{q}\lambda}(\tau_1, \tau_2) \mathcal{J}_{\mathbf{q}n_2} \right] = i\hbar \left[g_{\downarrow, n_1 n_2}(\tau_1, \tau_2) \Sigma_{\text{R}, n_1 n_2}(\tau_1, \tau_2) \right], \quad (\text{S21})$$

where the superscript 0 indicates that the phonon self-energy is evaluated using the noninteracting Green's function. Summing all higher-order contributions and including the left-lead self-energy $\Sigma_{\text{L}\uparrow, n_1 n_2}(\tau_1, \tau_2)$, we obtain the Dyson equation for $G_{\uparrow, mn}(\tau, \tau')$

$$G_{\uparrow, mn}(\tau, \tau') = g_{\uparrow, mn}(\tau, \tau') + \sum_{n_1 n_2} \iint_c d\tau_1 d\tau_2 \left[g_{\uparrow, mn_1}(\tau, \tau_1) \Sigma_{\uparrow, n_1 n_2}(\tau_1, \tau_2) G_{\uparrow, n_2 n}(\tau_2, \tau') \right], \quad (\text{S22})$$

where $\Sigma_{\uparrow, n_1 n_2}(\tau_1, \tau_2) = \Sigma_{\text{L}\uparrow, n_1 n_2}(\tau_1, \tau_2) + \bar{\Sigma}_{\text{R}\uparrow, n_1 n_2}^0(\tau_1, \tau_2)$. The left-lead electronic self-energy $\Sigma_{\text{L}\sigma}$ can be calculated numerically using an iterative algorithm [3, 4]. The phonon self-energy in Eq. (S21), evaluated with the noninteracting Green's function, corresponds to the lowest-order Born approximation. In our calculation, we first use Eq. (S21) to obtain the central-region Green's function with Eq. (S22), and then update the phonon self-energy by replacing the noninteracting Green's function with the newly obtained one. This procedure is repeated until convergence is reached. This is the self-consistent Born approximation and the corresponding Feynman diagrams are illustrated in Fig. S2.

Using the Langreth rules [1] and Fourier transforming to energy space, the Dyson and Keldysh equations in matrix form are expressed as

$$\mathbf{G}_{\uparrow}^{r/a}(E) = \mathbf{g}_{\uparrow}^{r/a}(E) + \mathbf{g}_{\uparrow}^{r/a}(E) \mathbf{\Sigma}_{\uparrow}^{r/a}(E) \mathbf{G}_{\uparrow}^{r/a}(E), \quad (\text{S23})$$

$$\mathbf{G}_{\uparrow}^{>/<}(E) = \mathbf{G}_{\uparrow}^r(E) \mathbf{\Sigma}_{\uparrow}^{>/<}(E) \mathbf{G}_{\uparrow}^a(E), \quad (\text{S24})$$

where $\mathbf{\Sigma}_{\uparrow}^{>/</r/a}(E) = \mathbf{\Sigma}_{\text{L}\uparrow}^{>/</r/a}(E) + \bar{\mathbf{\Sigma}}_{\text{R}\uparrow}^{>/</r/a}(E)$. The phonon self-energies $\bar{\mathbf{\Sigma}}_{\text{R}\uparrow}^{>/</r/a}(E)$ are given by

$$\bar{\Sigma}_{\text{R}\uparrow, ij}^>(E) = i \int \frac{d\omega}{2\pi} \left[G_{\downarrow, ij}^>(E - \hbar\omega) \Sigma_{\text{R}, ij}^>(\omega) \right], \quad (\text{S25})$$

$$\bar{\Sigma}_{\text{R}\uparrow, ij}^<(E) = i \int \frac{d\omega}{2\pi} \left[G_{\downarrow, ij}^<(E - \hbar\omega) \Sigma_{\text{R}, ij}^<(\omega) \right], \quad (\text{S26})$$

$$\bar{\Sigma}_{\text{R}\uparrow, ij}^r(E) = i \int \frac{d\omega}{2\pi} \left[G_{\downarrow, ij}^r(E - \hbar\omega) \Sigma_{\text{R}, ij}^<(\omega) + G_{\downarrow, ij}^>(E - \hbar\omega) \Sigma_{\text{R}, ij}^r(\omega) \right], \quad (\text{S27})$$

$$\bar{\Sigma}_{\text{R}\uparrow, ij}^a(E) = i \int \frac{d\omega}{2\pi} \left[G_{\downarrow, ij}^a(E - \hbar\omega) \Sigma_{\text{R}, ij}^<(\omega) + G_{\downarrow, ij}^>(E - \hbar\omega) \Sigma_{\text{R}, ij}^a(\omega) \right]. \quad (\text{S28})$$

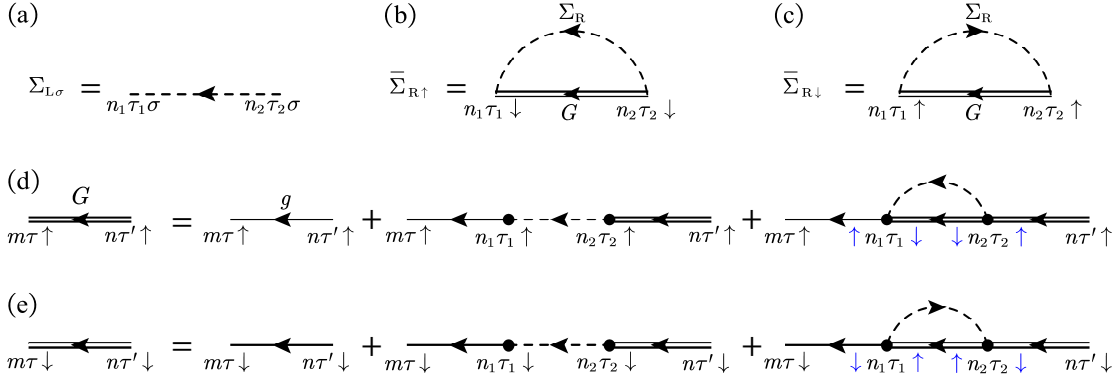


FIG. S2. Feynman diagrams for the electron self-energy $\Sigma_{L\sigma}$, the phonon self-energy $\bar{\Sigma}_{R\sigma}$ and the central-region Green's functions $G_{\sigma,mn}$. A single solid line with an arrow represents the noninteracting Green's function g , whereas a double solid line with an arrow represents the interacting Green's function G . A straight dotted line with an arrow denotes the left-lead self-energy $\Sigma_{L\sigma}$ and a curved dotted line with an arrow denotes the right-lead self-energy Σ_R . (a)-(c) Diagrams for the matrix elements of electronic self-energy $\Sigma_{L\sigma, n_1 n_2}(\tau_1, \tau_2)$, and the phononic self-energy $\bar{\Sigma}_{R\uparrow, n_1 n_2}(\tau_1, \tau_2)$ and $\bar{\Sigma}_{R\downarrow, n_1 n_2}(\tau_1, \tau_2)$, respectively. (d)-(e) Diagrams for the matrix elements of the fully interacting Green's functions $G_{\uparrow, mn}(\tau, \tau')$ and $G_{\downarrow, mn}(\tau, \tau')$, respectively. The filled black dots in (d) and (e) denote vertices to be integrated over. In the third term on the right-hand side of (d) and (e), the electron spin is flipped by phonon scattering, as indicated by the blue arrows.

Here $\mathbf{G}_{\downarrow}(E - \hbar\omega)$ is the Green's function for a spin \downarrow electron. The subscripts i and j label the matrix elements.

By an analogous derivation, we obtain the Dyson and Keldysh equations for a spin \downarrow Green's functions

$$\mathbf{G}_{\downarrow}^{r/a}(E) = \mathbf{g}_{\downarrow}^{r/a}(E) + \mathbf{g}_{\downarrow}^{r/a}(E) \Sigma_{\downarrow}^{r/a}(E) \mathbf{G}_{\downarrow}^{r/a}(E), \quad (\text{S29})$$

$$\mathbf{G}_{\downarrow}^{>/<}(E) = \mathbf{G}_{\downarrow}^r(E) \Sigma_{\downarrow}^{>/<}(E) \mathbf{G}_{\downarrow}^a(E), \quad (\text{S30})$$

where $\Sigma_{\downarrow}^{>/</r/a}(E) = \Sigma_{L\downarrow}^{>/</r/a}(E) + \bar{\Sigma}_{R\downarrow}^{>/</r/a}(E)$. The phonon self-energies $\bar{\Sigma}_{R\downarrow}^{>/</r/a}(E)$ are given by

$$\bar{\Sigma}_{R\downarrow, ij}^>(E) = i \int \frac{d\omega}{2\pi} \left[G_{\uparrow, ij}^>(E + \hbar\omega) \Sigma_{R, ji}^<(\omega) \right], \quad (\text{S31})$$

$$\bar{\Sigma}_{R\downarrow, ij}^<(E) = i \int \frac{d\omega}{2\pi} \left[G_{\uparrow, ij}^<(E + \hbar\omega) \Sigma_{R, ji}^>(\omega) \right], \quad (\text{S32})$$

$$\bar{\Sigma}_{R\downarrow, ij}^r(E) = i \int \frac{d\omega}{2\pi} \left[G_{\uparrow, ij}^r(E + \hbar\omega) \Sigma_{R, ji}^<(\omega) + G_{\uparrow, ij}^<(E + \hbar\omega) \Sigma_{R, ji}^a(\omega) \right], \quad (\text{S33})$$

$$\bar{\Sigma}_{R\downarrow, ij}^a(E) = i \int \frac{d\omega}{2\pi} \left[G_{\uparrow, ij}^a(E + \hbar\omega) \Sigma_{R, ji}^<(\omega) + G_{\uparrow, ij}^<(E + \hbar\omega) \Sigma_{R, ji}^r(\omega) \right]. \quad (\text{S34})$$

The relations between the left-lead self-energy $\Sigma_{L\sigma}(E)$ and the corresponding linewidth function $\Gamma_{L\sigma}(E)$ are [1]

$$\Sigma_{L\sigma}^>(E) = i[f_L(E) - 1]\Gamma_{L\sigma}(E), \quad \Sigma_{L\sigma}^<(E) = i f_L(E)\Gamma_{L\sigma}(E), \quad \Gamma_{L\sigma}(E) = i[\Sigma_{L\sigma}^r(E) - \Sigma_{L\sigma}^a(E)], \quad (\text{S35})$$

where $f_L(E) = [e^{(E - \mu_L)/(k_B T_L)} + 1]^{-1}$ is the Fermi-Dirac distribution. We model the right phonon reservoir with a super-Ohmic spectral density [5-7]

$$J_R(\omega) = \alpha \hbar \frac{\omega^3}{\omega_0^2} e^{-\omega/\omega_0}, \quad (\text{S36})$$

where the dimensionless parameter α describes the dissipation into the reservoir and $\hbar\omega_0$ is the cutoff energy. The right-lead linewidth function is taken to be $\Gamma_R(\omega) = J_R(\omega)\mathbf{I}$. The relations between the right-lead self-energy $\Sigma_R(\omega)$ and $\Gamma_R(\omega)$ are [1]

$$\Sigma_R^>(\omega) = -i[n_R(\omega) + 1]\Gamma_R(\omega), \quad \Sigma_R^<(\omega) = -i n_R(\omega)\Gamma_R(\omega), \quad \Sigma_R^r(\omega) = [\Sigma_R^a(\omega)]^\dagger = -i\Gamma_R(\omega)/2, \quad (\text{S37})$$

where $n_{\text{R}}(\omega) = [e^{(\hbar\omega)/(k_{\text{B}}T_{\text{R}})} - 1]^{-1}$ is the Bose–Einstein distribution. Using Eq. (S1) and Eq. (S13), the spin current in the left lead is expressed as

$$\begin{aligned} I_{\text{s}} &= \frac{\hbar}{2e} (I_{\uparrow}^e - I_{\downarrow}^e) = \frac{\hbar}{2e} (I_{\uparrow}^e + I_{\uparrow}^e) = \frac{\hbar}{e} I_{\uparrow}^e \\ &= \int \frac{dE}{2\pi} \text{Tr} \left\{ \mathbf{G}_{\uparrow}^r(E) \left[i f_{\text{L}}(E) \overline{\Sigma}_{\text{R}\uparrow}^>(E) + i(1 - f_{\text{L}}(E)) \overline{\Sigma}_{\text{R}\uparrow}^<(E) \right] \mathbf{G}_{\uparrow}^a(E) \Gamma_{\text{L}\uparrow}(E) \right\}. \end{aligned} \quad (\text{S38})$$

For an insulating electronic system, $I_{\uparrow}^e = -I_{\downarrow}^e$ and therefore, for simplicity, we consider only the spin-up contribution here.

S3. THE EXPRESSION OF THE PHONON ANGULAR MOMENTUM CURRENT IN THE RIGHT LEAD

In what follows, we derive the expression of the pAM current in the right lead. The phonon number operator of the right lead is expressed as $N_{\text{R}} = \sum_{\mathbf{q}\lambda} a_{\mathbf{q}\lambda}^{\dagger} a_{\mathbf{q}\lambda}$, where $\lambda = \pm$ labels the phonon chirality. We define \mathcal{N}_{R} as the difference between the phonon numbers of opposite chiralities as

$$\mathcal{N}_{\text{R}} = \sum_{\mathbf{q}} (a_{\mathbf{q}+}^{\dagger} a_{\mathbf{q}+} - a_{\mathbf{q}-}^{\dagger} a_{\mathbf{q}-}). \quad (\text{S39})$$

The pAM current is

$$I_{\text{ph}} = \hbar \left\langle \frac{d}{dt} \mathcal{N}_{\text{R}} \right\rangle = \hbar \sum_m \{ [G_{m,+}^<(t, t) - G_{m,-}^<(t, t)] + \text{h.c.} \}, \quad (\text{S40})$$

where the lesser Green's functions are defined as

$$G_{m,+}^<(t, t') = -\frac{i}{\hbar} \sum_{\mathbf{q}} \mathcal{J}_{\mathbf{q}m} \langle d_{\mathbf{q}+}^{\dagger}(t') c_{m\downarrow}^{\dagger}(t) c_{m\uparrow}(t) \rangle, \quad G_{m,-}^<(t, t') = -\frac{i}{\hbar} \sum_{\mathbf{q}} \mathcal{J}_{\mathbf{q}m} \langle d_{\mathbf{q}-}^{\dagger}(t') c_{m\downarrow}^{\dagger}(t) c_{m\uparrow}(t) \rangle. \quad (\text{S41})$$

We then introduce the corresponding contour-ordered Green's functions

$$G_{m,+}(\tau, \tau') = -\frac{i}{\hbar} \sum_{\mathbf{q}} \mathcal{J}_{\mathbf{q}m} \langle \mathcal{T}_c \mathcal{S} c_{m\downarrow}^{\dagger}(\tau) c_{m\uparrow}(\tau) d_{\mathbf{q}+}^{\dagger}(\tau') \rangle_0, \quad (\text{S42})$$

$$G_{m,-}(\tau, \tau') = -\frac{i}{\hbar} \sum_{\mathbf{q}} \mathcal{J}_{\mathbf{q}m} \langle \mathcal{T}_c \mathcal{S} c_{m\downarrow}^{\dagger}(\tau) c_{m\uparrow}(\tau) d_{\mathbf{q}-}^{\dagger}(\tau') \rangle_0. \quad (\text{S43})$$

Using a similar procedure for the perturbative expansion as that used in the previous section, we obtain

$$\begin{aligned} G_{m,\pm}^<(t, t) &= G_{m,+}(t, t) - G_{m,-}(t, t) \\ &= \frac{1}{\hbar} \sum_{m_1} \int \frac{dE}{2\pi} [g_{\uparrow, mm_1}^r(E) \overline{\Sigma}_{\text{R}, m_1 m}^<(E) + g_{\uparrow, mm_1}^<(E) \overline{\Sigma}_{\text{R}, m_1 m}^a(E)] \end{aligned} \quad (\text{S44})$$

where

$$\overline{\Sigma}_{\text{R}, m_1 m}^<(E) = i \int \frac{d\omega}{2\pi} [g_{\downarrow, m_1 m}^<(E - \hbar\omega) \Sigma_{\text{R}, m_1 m}^<(\omega)], \quad (\text{S45})$$

$$\overline{\Sigma}_{\text{R}, m_1 m}^a(E) = i \int \frac{d\omega}{2\pi} [g_{\downarrow, m_1 m}^a(E - \hbar\omega) \Sigma_{\text{R}, m_1 m}^<(\omega) + g_{\downarrow, m_1 m}^>(E - \hbar\omega) \Sigma_{\text{R}, m_1 m}^a(\omega)]. \quad (\text{S46})$$

Likewise, we model the right phonon reservoir with a super-Ohmic spectral density given in Eq. (S36). In the end, the pAM current is

$$I_{\text{ph}} = \int \frac{dE}{2\pi} \text{Tr} \left\{ \mathbf{G}_{\uparrow}^r(E) \Gamma_{\text{L}\uparrow}(E) \mathbf{G}_{\uparrow}^a(E) [2f_{\text{L}}(E) \text{Im} \overline{\Sigma}_{\text{R}}^r(E) - i \overline{\Sigma}_{\text{R}}^<(E)] \right\}. \quad (\text{S47})$$

S4. VERIFICATION OF CURRENT CONSERVATION

The spin current is usually not conserved in the presence of the spin-orbit interaction (SOI) [8–10]. For simplicity, we neglect the SOI-induced spin nonconservation in the NM, since our primary focus is the generation of spin current via spin-phonon conversion. Accordingly, the spin current I_s in the left lead should be equal in magnitude to the phonon angular momentum current I_{ph} in the right lead, i.e., $I_s = I_{\text{ph}}$. The current conservation is verified numerically in Fig. S3.

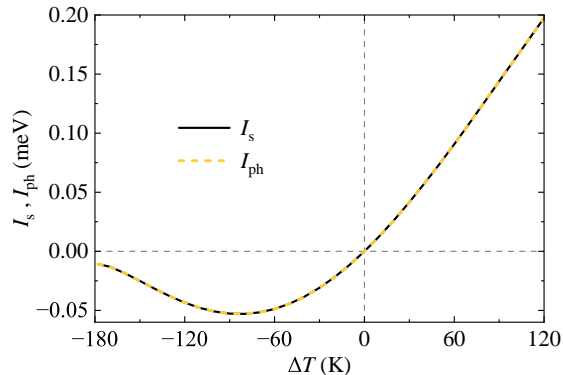


FIG. S3. Spin current I_s (blue solid line) and phAM current I_{ph} (orange dotted line) plotted as functions of the temperature difference ΔT . Other parameters: $T_0 = 90$ K, $\mu_L = 1$ meV, $\alpha = 5$ and $\hbar\omega_0 = 7$ meV.

S5. THE LATTICE HAMILTONIAN OF THE NORMAL METAL

In this section, we present the tight-binding Hamiltonian of the normal metal. We focus on the 3D case; the 1D and 2D cases can be obtained by a similar procedure. We begin with the Hamiltonian with only the kinetic energy of N_e electrons

$$H_{3\text{D}} = \sum_{i=1}^{N_e} \frac{\hat{\mathbf{p}}_i^2}{2m} = -\frac{\hbar^2}{2m} \sum_{i=1}^{N_e} \nabla_i^2. \quad (\text{S48})$$

The single-electron wave function is $\phi_{\mathbf{k}\sigma}(\mathbf{r}) = (1/\sqrt{V}) e^{i\mathbf{k}\cdot\mathbf{r}}|\sigma\rangle$, where \mathbf{k} is the wave vector and σ denotes the spin. The Hamiltonian in second-quantized form is

$$H_{3\text{D}} = \sum_{\mathbf{k}\sigma} \sum_{\mathbf{k}'\sigma'} \langle \mathbf{k}'\sigma' | \frac{\hat{\mathbf{p}}^2}{2m} | \mathbf{k}\sigma \rangle c_{\mathbf{k}'\sigma'}^\dagger c_{\mathbf{k}\sigma} = \sum_{\mathbf{k}\sigma} \frac{\hbar^2 k^2}{2m} c_{\mathbf{k}\sigma}^\dagger c_{\mathbf{k}\sigma}, \quad (\text{S49})$$

Considering the replacement $k_i^2 \rightarrow (2/a^2)[1 - \cos(k_i a)]$ and performing the Fourier transform of the creation and annihilation operators with

$$c_{\mathbf{k}\sigma} = \frac{1}{\sqrt{V}} \sum_i e^{i\mathbf{k}\cdot\mathbf{r}_i} c_{i\sigma}, \quad c_{\mathbf{k}\sigma}^\dagger = \frac{1}{\sqrt{V}} \sum_i e^{-i\mathbf{k}\cdot\mathbf{r}_i} c_{i\sigma}^\dagger, \quad (\text{S50})$$

we obtain

$$H_{3\text{D}} = 6t \sum_{i\sigma} c_{i\sigma}^\dagger c_{i\sigma} - t \sum_{\langle ij \rangle \sigma} c_{i\sigma}^\dagger c_{j\sigma}, \quad (\text{S51})$$

where we have defined $t = \hbar^2/(2ma^2)$. Here i labels lattice sites and $\langle ij \rangle$ denotes nearest-neighbor hopping. For 1D and 2D cases, we have

$$H_{1\text{D}} = 2t \sum_{i\sigma} c_{i\sigma}^\dagger c_{i\sigma} - t \sum_{\langle ij \rangle \sigma} c_{i\sigma}^\dagger c_{j\sigma}, \quad (\text{S52})$$

$$H_{2\text{D}} = 4t \sum_{i\sigma} c_{i\sigma}^\dagger c_{i\sigma} - t \sum_{\langle ij \rangle \sigma} c_{i\sigma}^\dagger c_{j\sigma}. \quad (\text{S53})$$

In this work, both the left lead and the central region are modeled as a normal metal described by the tight-binding Hamiltonian above with the hopping parameter $t = 21.768$ meV.

S6. THE SPIN CURRENT FOR DIFFERENT CENTRAL-REGION SIZES AND DIMENSIONALITIES

In the main text, we model the central region as a quantum dot for simplicity. Here we present the calculated spin current for different central-region sizes using the 2D and 3D lattice Hamiltonians given in Eqs. (S53) and (S51), respectively. The results, shown in Figs. S4(a)-S4(b), demonstrate that the negative differential SSE also persists in 2D and 3D systems, although the magnitude of the spin current depends on the dimensionality and the central-region size.

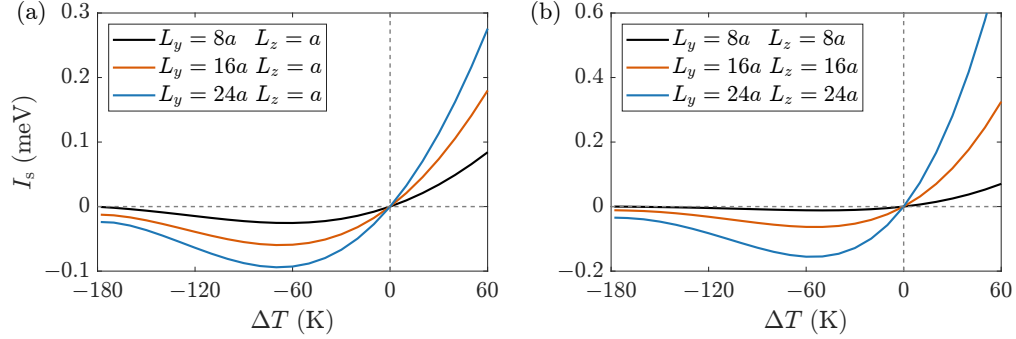


FIG. S4. Spin current I_s as a function of the temperature difference ΔT for different central-region sizes. The width of the central region along the transport direction is fixed at $L_x = a$, where $a = 5$ nm is the lattice constant. Other parameters are $T_0 = 90$ K, $\alpha = 5$, and $\hbar\omega_0 = 7$ meV. The chemical potential of the left lead is set to (a) $\mu_L = 3$ meV for the 2D model and (b) $\mu_L = 6$ meV for the 3D model.

* gmtang@gscaep.ac.cn

† xingyanxia@bit.edu.cn

- [1] H. Haug and A.-P. Jauho, *Quantum kinetics in transport and optics of semiconductors* (Springer, 2008).
- [2] T. Funato, M. Matsuo, and T. Kato, Chirality-induced phonon-spin conversion at an interface, *Phys. Rev. Lett.* **132**, 236201 (2024).
- [3] M. P. L. Sancho, J. M. L. Sancho, and J. Rubio, Quick iterative scheme for the calculation of transfer matrices: application to Mo (100), *J. Phys. F: Met. Phys.* **14**, 1205 (1984).
- [4] M. P. L. Sancho, J. M. L. Sancho, and J. Rubio, Highly convergent schemes for the calculation of bulk and surface Green functions, *J. Phys. F: Met. Phys.* **15**, 851 (1985).
- [5] U. Weiss, *Quantum Dissipative Systems* (WORLD SCIENTIFIC, 2008).
- [6] M. Thorwart, J. Eckel, and E. R. Mucciolo, Non-Markovian dynamics of double quantum dot charge qubits due to acoustic phonons, *Phys. Rev. B* **72**, 235320 (2005).
- [7] Q.-S. Tan, W. Wu, L. Xu, J. Liu, and L.-M. Kuang, Quantum sensing of supersensitivity for the Ohmic quantum reservoir, *Phys. Rev. A* **106**, 032602 (2022).
- [8] J. Wang, B. Wang, W. Ren, and H. Guo, Conservation of spin current: Model including self-consistent spin-spin interaction, *Phys. Rev. B* **74**, 155307 (2006).
- [9] Q.-f. Sun and X. C. Xie, Definition of the spin current: The angular spin current and its physical consequences, *Phys. Rev. B* **72**, 245305 (2005).
- [10] J. Shi, P. Zhang, D. Xiao, and Q. Niu, Proper Definition of Spin Current in Spin-Orbit Coupled Systems, *Phys. Rev. Lett.* **96**, 076604 (2006).